New insights on regional tectonics and basement composition beneath the eastern Sierras Pampeanas (Argentine back-arc region) from seismological and gravity data

Jean-Baptiste Ammirati[a,*], Agostina Venerdini[a,b], Juan Manuel Alcacer[b], Patricia Alvarado[a,b], Silvia Miranda[b], Hersh Gilbert[c]

[a] CIGEOBIO-CONICET, Universidad Nacional de San Juan, Argentina
[b] Departamento de Geofísica y Astronomía, Facultad de Ciencias Exactas, Físicas y Naturales, Universidad Nacional de San Juan, Argentina
[c] Department of Geosciences, University of Calgary, Canada

A B S T R A C T

The eastern Sierras Pampeanas (ESP) are the easternmost expression of a series of foreland uplifts in the Argentine back arc region (~30–34°S) and show spatial and temporal connections with the subduction of the Juan Fernández Ridge (JFR) under the South American plate. In order to get new insights on the mechanisms that control crustal regional tectonics, we computed teleseismic receiver functions (RF) and jointly invert them with Rayleigh-wave phase velocity dispersion curves. RFs allow resolving crustal thickness and intra crustal velocity variations with a good vertical resolution whereas surface wave information helps to constrain absolute seismic wave velocities.

Our seismic images have been combined with crustal density modeling in order to further investigate if the shear wave velocity structure obtained from the RF-SW joint inversion could explain the observed gravity variations. Our results show a crustal thickness varying from 35–40 km (east) to 45–50 km (west) with a Moho step at ~66°W. This step regionally presents a NW-SE orientation and is parallel to the trace at the surface of the Valle Fértil–La Huerta (VFLH) lineament (Cuyania-Pampia boundary). Our images also reveal the presence of a high wave velocity (high density) lower crust west of this Moho step, beneath the eastern Sierras Pampeanas (at 66–67°W). This observation suggests the east-dipping extension at depth of the VFLH structure and the underthrusting of the Cuyania lower crust under the Pampia terrane along this structure. Finally, we evidenced localized low velocity zones located at about 10 km beneath late Cenozoic volcanic fields (Pocho, Morro). We believe that these low velocity zones correspond to old magma chambers associated to the recent, slab flattening-related volcanism in the ESP.

1. Introduction and geological setting

Observations resulting from geological (Stauder, 1973; Ramos, 1988; Kay and Abbruzzi, 1996; Ramos et al., 2002) and geophysical investigations (Barazangi and Isacks, 1976; Cahill and Isacks, 1992; Anderson et al., 2007; Mulcahy et al., 2014) have produced constraints on along strike variations in the angle of subduction including the Chilean-Pampean flat slab segment (Fig. 1). The flat slab subduction has been related to the subduction of the Juan Fernandez Ridge (JFR), a submarine volcano chain located on top of the Nazca plate (Yáñez et al., 2002), as the geometry of the Nazca plate under the South American plate matches the projected orientation of the JFR.

At the surface, the Argentine back-arc region is characterized by three main structural units (Fig. 1). These units are the Pampia terrane to the east, where the eastern Sierras Pampeanas (ESP) are located, the Cuyania terrane in the middle, containing the Precordillera (PC) and western Sierras Pampeanas (WSP), and the Chilenia terrane to the west, forming the basement of the principal and frontal Cordillera (PFC).

The regional tectonics involves a three-stage evolutional history that included accretion during the Famatinian orogeny (Early Ordovician to Early Cretaceous), extension during the Gondwanic cycle (Early Carboniferous to Early Cretaceous), and compression again, during the Andean orogeny (Early Cretaceous to present) (Ramos, 1988) that reactivated and inverted previous accretionary structures. As a result, a
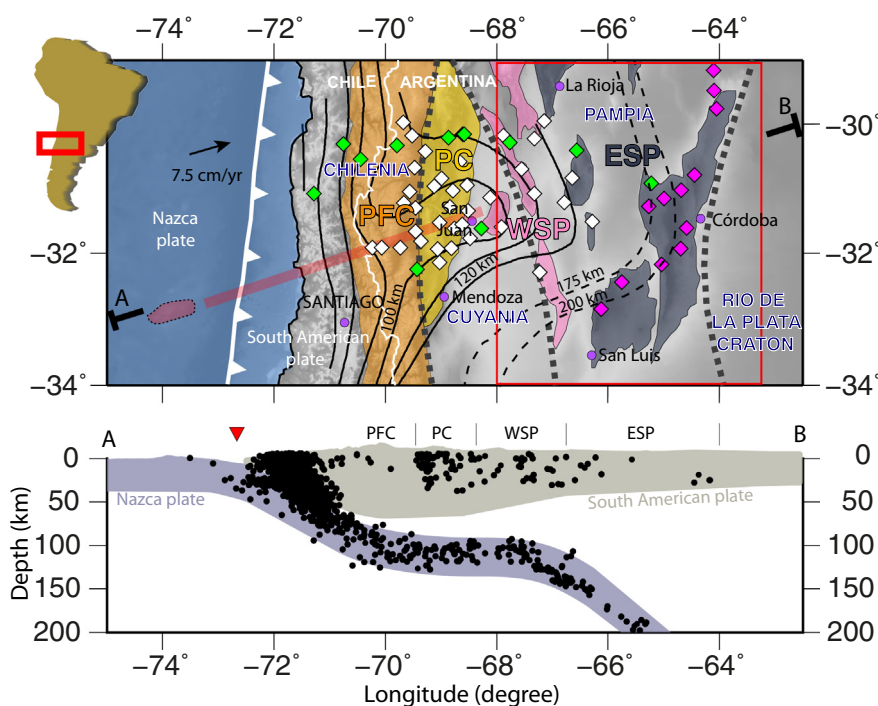
Fig. 1. (top) Location map centered on the flat slab region of the South Central Andes. Thick dashed lines mark terrane boundaries (Ramos et al., 2002; Rapela et al., 2011). Slab top contours are shown by thin black lines (Anderson et al., 2007) and thin black dashed lines (Mulcahy et al., 2014). Locations of the different seismic stations deployed in the region are marked by the green (CHARGE), white (SIEMBRA) and pink (ESP) diamonds. The red thick line shows the path of the JFR subducting under the South American plate (Yáñez et al., 2002). The convergence orientation and rate between the Nazca plate and the South American plate is from DeMets et al. (2010). The red rectangle delimitates our study region. Main cities and localities from both countries are shown by magenta circles. (bottom) Cross-section A-B showing intra slab and intra crustal seismic locations (Marot et al., 2013). PFC: Principal and Frontal Cordillera; PC: Precordillera; WSP: western Sierras Pampeanas; ESP: eastern Sierras Pampeanas (Ramos, 1988). (For interpretation of the references to color in this figure legend, the reader is referred to the web version of this article.)

series of thin-skinned and basement-cored uplifts extends up to 700 km east from the Nazca-South America trench in the Precordillera and the Sierras Pampeanas. Those three main accreted units exhibit seismic activity mostly along their suture zones (Brooks et al., 2003; Alvarado et al., 2007; Ammirati et al., 2015, 2016). Among those structures, a NW-SE oriented suture zone bounding the western flank of the Valle Fértil–La Huerta range (VFLH) (western Sierras Pampeanas) extends about 600 km, marking the transition at the surface between the terranes Cuyania (west) and Pampia (east) (Snyder et al., 1990; Ramos et al., 2002; Otamendi et al., 2009). Recent termochronological, neotectonic and geophysical studies indicate that this structure seems to play a major role in the uplift of the western Sierras Pampeanas (Ortiz et al., 2015).

The eastern Sierras Pampeanas (ESP) between 29°S to 34°S and 64°W to 67°W (Figs. 1 & 2a) represent the easternmost manifestation of crustal shortening for which the deformation mainly consists of tilted basement blocks bounded to the west by high dipping reverse faults (Ramos et al., 2010). The resulting ranges thus present an asymmetric shape, stretched along the N-S direction with a steep western flank and a low-angle slope on their eastern side. Although the deformation of the eastern Sierras Pampeanas mainly affects rocks of Neoproterozoic to early Paleozoic ages (Fig. 2a), geologic evidence shows that the uplifting began much more recently, during the Miocene, by the tectonic inversion of Cretaceous faults (Siegesmund et al., 2010; Martino et al., 2016). The uplift of the eastern Sierras Pampeanas appears to be synchronized with the flattening of the Nazca plate, as evidenced by the eastward migration of arc volcanism during the past 15 Ma (Kay and Abbruzzi, 1996). Seismological and resistivity studies (Cahill and Isacks, 1992; Booker et al., 2004; Mulcahy et al., 2014) detected what appears to be the top of the slab lying around 175 km depth beneath the Sierras de Córdoba in the ESP (Figs. 1 & 2a). Observations and dating of volcanic rocks show volcanic activity in the central portion of the ESP ~4.7 Ma in the Sierra de Pocho at ~31°S (Gordillo and Linares, 1981; Kay and Gordillo, 1994) and ~1.9 Ma in the southern ESP, in the Sierra de San Luis (El Morro) at ~33°S (Urbina et al., 1997) (Fig. 2a).

Recent seismicity records and historical earthquakes (INPRES, 2018) show that this region is currently active within both upper and lower plate levels (Fig. 1). The general objective of this study is to determine an improved lithospheric velocity structure in the eastern

Sierras Pampeanas involving crustal details, to better understand the regional tectonics, their connection with the western Sierras Pampeanas and the flat subduction of the Nazca plate. In the future, our improved velocity structure could be used to improve the seismic characterization of shallow events in this region.

2. Previous geophysical studies

This study uses data from three seismic experiments deployed between 2000 and 2010 (Fig. 1); The **CH**ile **AR**gentina **G**eophysical **E**xperiment (CHARGE) from November 2000 to August 2002; The **SI**erras Pampeanas **E**xperiment using a **M**ulticomponent **BR**oadband **A**rray (SIEMBRA) from December 2007 to December 2009 and the **E**astern **S**ierras **P**ampeanas experiment (ESP) from September 2008 to August 2010. Those experiments were deployed in the Pampean flat slab region to investigate relationships between the subducting Nazca Plate and the crustal shortening observed at the surface (Figs. 1 & 2).

Using P- and S-wave traveltime tomography, Wagner et al. (2005) constrained the wave velocity within the subducting Nazca plate and the overlying mantle. Their findings, later confirmed by Porter et al. (2012) using a combination of earthquake generated surface wave and Ambient Noise Tomography (ANT), evidenced that the subducting plate geometry seems to control the water content and temperature of the overlying mantle wedge. In particular, the region exhibits a hydrated slab and a dry overlying mantle wedge within the flat portion of the slab (beneath the Precordillera) and a dry slab with a hydrated overlying mantle wedge beneath the ESP (Wagner et al., 2005; Alvarado et al., 2007; Porter et al., 2012).

Receiver function (RF) observations from the Pampean flat slab region found the crust to be 50 km thick beneath the western Sierras Pampeanas, > 60 km beneath the Precordillera and ~70 km thick beneath the Frontal and Principal Cordillera (Gilbert et al., 2006; Calkins et al., 2006; Perarnau et al., 2010; Gans et al., 2011; Ammirati et al., 2013, 2015). In addition to these RF results, other studies that used a range of seismic methods observed similar crustal thicknesses (Regnier et al., 1992; Alvarado et al., 2007; McGlashan et al., 2008).

The seismic velocity structure combined with petrological analyses (Pérez Luján et al., 2015) provided evidence that the composition of the Cuyania basement consists of dense mafic to ultramafic rocks, which
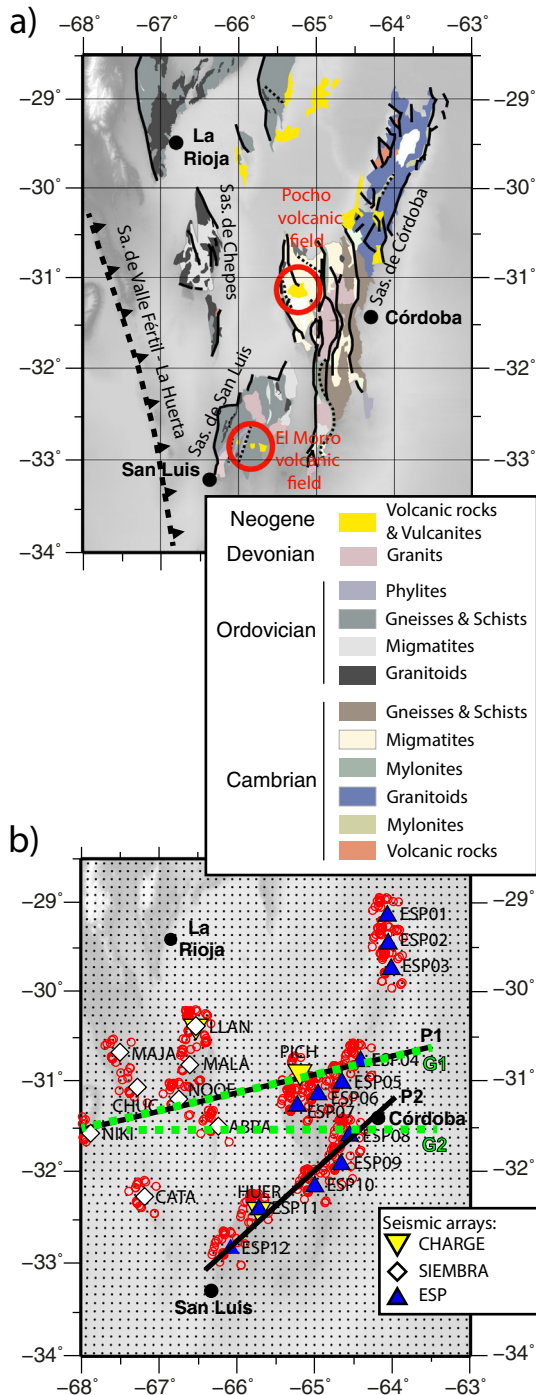
Fig. 2. a) Map of the study region showing main geological units and structures according to geological information from Lucero-Michaut et al. (1995). b) Location of the seismic stations used in this work to compute teleseismic receiver functions and Rayleigh-wave phase velocity dispersion curves. Black lines mark the location of the CCP stacked RF cross-sections shown in Fig. 4. The red circles show the RF piercing points at 40 km depth. Small black dots mark bin centers for common conversion point (CCP) stacks. Gravity cross-sections realized in this work are shown as green dashed lines (Fig. 7). (For interpretation of the references to color in this figure legend, the reader is referred to the web version of this article.)

could explain how a region of relatively low average elevation (~2500 m) has such thick crust (Alvarado et al., 2009). Seismic observations from the eastern Sierras Pampeanas (Alvarado et al., 2007; Perarnau et al., 2012; Richardson et al., 2013; Ammirati et al., 2015)

show that the crust is thinner (~40 km) and the crustal wave velocities are lower than those observed beneath the western Sierras Pampeanas and the Precordillera (Alvarado et al., 2007; Ammirati et al., 2013; Venerdini et al., 2016). Gravity models for this region, estimated the Moho depth at 39.5 km beneath the Sierras de Córdoba (Miranda and Introcaso, 1999). This study was based on gravity data collected along an east–west profile at 31.5°S that extended from the Andes foothills to the easternmost boundaries of the Sierras Pampeanas (Fig. 2b).

Crustal seismicity in the ESP appears to be horizontally distributed between depths of 15 and 25 km (Richardson et al., 2012). The solutions of available focal mechanisms for small-to-moderate magnitude events are heterogeneous, although they consistently exhibit some shear component (Alvarado et al., 2005; Richardson et al., 2012). Using local RF analysis, Perarnau et al. (2012) examined the crustal velocity structure and identified major faults within the Pampia basement. These faults seem to extent from the surface to a regional décollement level at about 20 km depth, which seems to align with the distribution of seismicity (Richardson et al., 2012).

Here, we refine these earlier models of the regional velocity structure through joint inversions of RFs and Rayleigh-wave dispersion data. In addition, we use constraints from gravity data for the eastern Sierras Pampeanas to build a 2D lithospheric profile and address the hypothesis derived from the interpretations of our seismic results. The updated velocity structure developed in this work helps us to discuss the evolution of the ESP and could be used in future regional seismic studies.

3. Data and methods

Discontinuities in seismic velocities generate P-to-S-wave conversions. Because of differences in the velocities of P- and S-waves, the arrival time of the converted S-waves following the direct P is sensitive to the depth where it originated as well as the velocities of the waves. The discontinuity structure beneath three-component seismometers can be measured using these converted S-waves once the signal from P-waves has been removed (Langston, 1979). This separation produces a receiver function and is accomplished by deconvolving the vertical seismogram from the radial or tangential. Because RFs are only sensitive to discontinuities in seismic velocities, solving for the depths of those discontinuities is inherently non-unique (Ammon et al., 1990). However, jointly inverting RFs and Rayleigh-wave phase velocities, which are sensitive to shear wave velocities, can be used to overcome this limitation (Julià et al., 2000).

3.1. Receiver functions

RFs were calculated using events in the USGS-NEIC catalog (https://earthquake.usgs.gov/earthquakes/) with Mw ≥ 6.0 and epicentral distances between 25 and 95° (Fig. 3a) ensuring traces presenting a high signal-to-noise ratio (SNR). The first P-wave arrival has been manually picked allowing to visualize the seismograms and discard traces with low SNR, gaps on any recording artifact. Prior to processing, the mean has been removed from the seismograms and a symmetric taper has been applied at both ends of the data. The traces have been cut within an 80 s time window (20 s before first P-wave arrival and 60 s after). The three-component seismograms were then band-pass filtered between 0.15 and 5 Hz to remove unwanted long- and short-period signals. The traces were then rotated to their great circle path coordinates. Following these steps, radial and tangential RFs were computed in the time domain using an iterative method (Ligorría and Ammon, 1999). The iterative deconvolution was limited to 400 iterations or once the fit of the RF did not improve by > 0.01%. The RFs were calculated using a Gaussian value of 2.5 (corresponding to low-pass filter with a corner frequency of ~1.2 Hz) to remove unwanted high-frequency signals and noise. This process yielded 1203 radial RFs. We used the FUNCLAB package (Eagar and Fouch, 2012) to visualize the RFs obtained at each station and perform further quality control. Thus, RFs with a variance
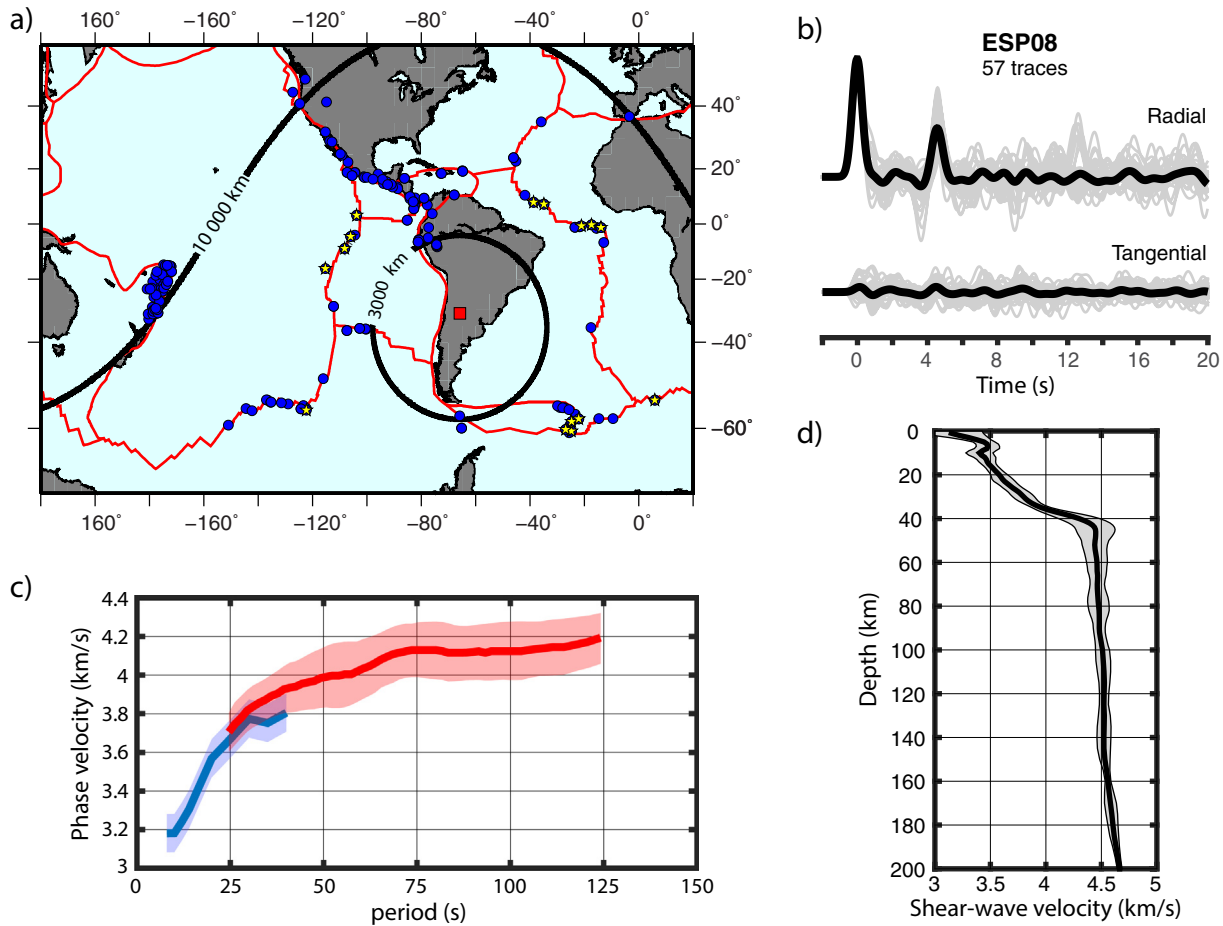
Fig. 3. a) Epicentral location of the teleseismic earthquakes used in this work, which were recorded by the seismic experiments shown in Fig. 2b. The red square marks the location of the study area. Red lines are tectonic plate boundaries. Yellow stars denote the earthquakes used to calculate the long-period (20–120 s) Rayleigh-wave dispersion curves (see main text). b) Radial and tangential receiver functions obtained for station ESP08 (Fig. 2b). In both cases, individual RFs (grey) are corrected from moveout and stacked (black). Note how the tangential RFs present much lower amplitude than the radial RFs. c) Phase velocity dispersion data for station ESP08. The blue line (and estimated error of 0.08 km/s) is extracted from the ambient noise tomography model obtained by Porter et al. (2012), the red line is the regional phase velocity dispersion obtained in this work with confidence bounds (one standard deviation). d) Regional velocity model obtained from the joint inversion RFs and phase velocity dispersion. Individual velocity models obtained for each station are averaged (black line). The grey envelope shows the uncertainty of resulting shear wave velocities within one standard deviation value. (For interpretation of the references to color in this figure legend, the reader is referred to the web version of this article.)

reduction < 80%, an inconsistent negative first P-wave arrival, or harmonic signals were discarded. A total of 624 radial RFs passed the quality control and were used for the subsequent stages of analysis. Tangential RFs have also been computed in order to compare their amplitudes with the corresponding radial RFs. The sampling region can only be assumed to be close to homogeneous and isotropic when the tangential RF amplitudes are significantly lower than the radial RF amplitudes, which can be observed in Figs. 3b & S1.

3.2. Phase velocities

In this study we use Rayleigh-wave phase velocity dispersion within the 8–120 s period range. Dispersion data with period from 8 to 40 s come from the ambient noise tomography (ANT) by Porter et al. (2012) (Fig. S2). Rayleigh-waves at these short periods are mostly sensitive to crustal velocities. For longer periods, the phase velocity dispersion has been estimated using a similar methodology to Ammirati et al. (2015). Briefly, this method applies a phase match filter (Herrmann, 1973) to 15 selected (Mw ≥ 6) teleseismic earthquakes that present high signal-to-noise ratios (Fig. 3a). The phase match filter allows isolating the fundamental mode Rayleigh wave within the 25–120 s period resulting in "clean" waveforms with no interference from body waves and higher

modes. For each event, we then use a wavefield transformation method (McMechan and Yeldin, 1981) to build an average dispersion curve for the entire network. This process is performed in the frequency domain and yields a dispersion curve for each of the 15 events (Fig. S3). These curves are then stacked to produce our final regional phase velocity dispersion curve (Fig. 3b). The ambient noise phase velocities were then combined with our longer ($25 < T < 120$ s) period observations from earthquakes (Fig. 3a) and used in the joint receiver function inversion.

3.3. Joint inversion and CCP stacking

The joint inversion of RFs and Rayleigh wave phase velocities is performed using the joint96 code (Julià et al., 2000; Herrmann and Ammon, 2002) where an initial velocity model is iteratively updated in order to fit both datasets. Just as used by other studies (e.g., Porter et al., 2012) we use a homogenous initial model comprised of layers with a Vs of 4 km/s and a Vp/Vs = 1.75 from depths of 0 to 150 km. The use of a constant model at these shallow depths avoids retaining any a priori discontinuities in the final model. At depths from 150 to 400 km, the starting model uses velocities from the AK135 global reference model (Kennett et al., 1995) to avoid mapping deep velocities into shallower structure (Julià et al., 2008). Layers in the initial model
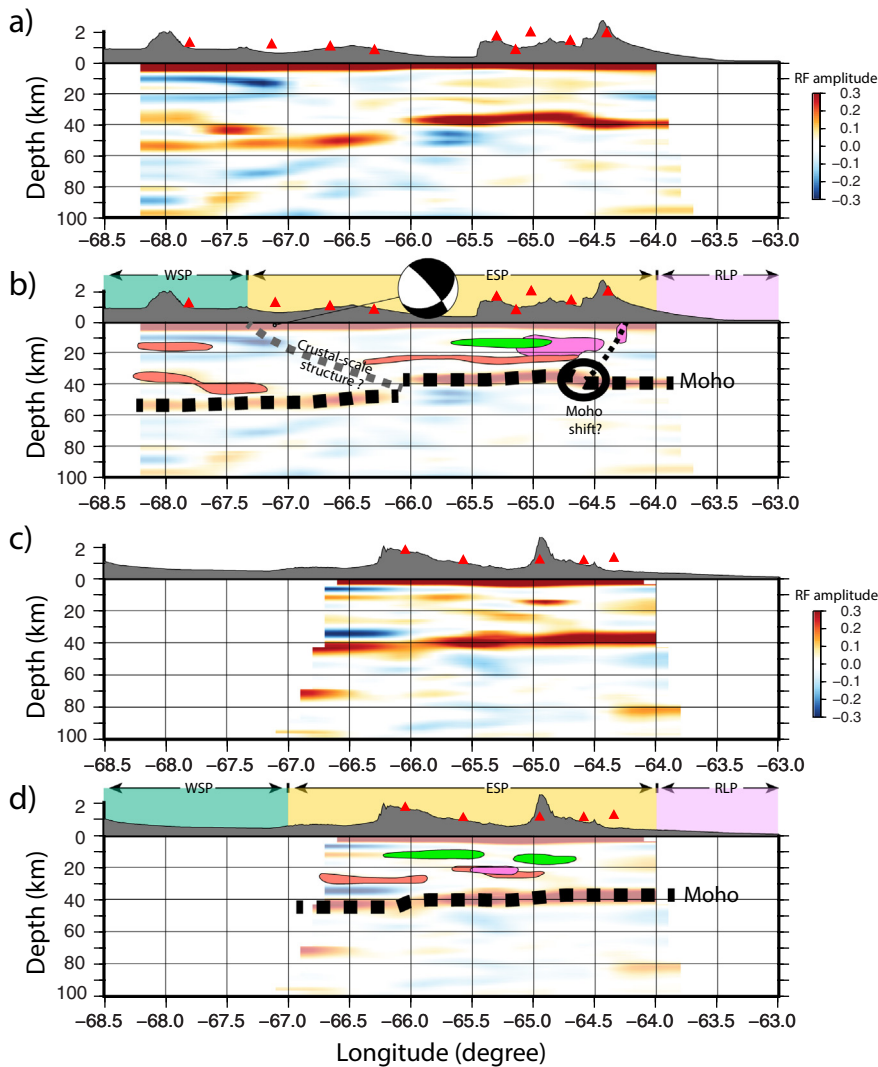
Fig. 4. Cross-sections P1 and P2 (see locations in Fig. 2b) showing our CCP stacked RFs. (a) and (c) show raw RF results for P1 and P2 cross-sections, respectively whereas the corresponding interpretations are shown in (b) and (d). RF positive amplitudes are in red, negative amplitudes are in blue. Red triangles are the seismic stations for which RFs were computed. Our interpretations for the Moho signal correspond to the black dashed lines. Note the change in Moho depth at ~66°W. The focal mechanism in (b) corresponds to a shallow (2009-07-02) Mw 4.2 earthquake determined by Ammirati et al. (2015) using regional seismic moment tensor inversion. The mechanism is consistent with reverse faulting at the transition between the WSP and the ESP. The dashed grey line shows the possible extension at depth of the VFLH fault (see main text). Red regions highlight the intra-crustal discontinuities interpreted as décollement levels. Pink areas show seismogenic zones beneath the Sierras de Córdoba (ESP) from Richardson et al. (2012). Green areas correspond to our interpretations for lateral lithology changes (see main text). (For interpretation of the references to color in this figure legend, the reader is referred to the web version of this article.)

are 1-km thick for depths between 0 and 50 km, 2-km between 50 and 100 km and 10-km for layers deeper than 100 km. A damping factor of 0.4 was selected as the best compromise between data fit quality and abrupt, unrealistic changes in wave velocities in the resulting model (Fig. S4). The joint inversion assigns a weight of 25% to the surface wave (SW) observations and 75% to the receiver functions. These values were chosen based on a broader range of models being able to fit the SW observation and the RFs are able to provide needed constraints on the distribution of discontinuities within those models. Therefor assigning more weight to the SW observations would lead the inversion to produce smoother models. For our processing each RFs is inverted individually, which results in one velocity model for each RF. Those models are then averaged to produce a shear wave velocity model for that station (Fig. S5). This averaging introduces additional smoothing for the station models. Combining the results of the 18 1D velocity models (Fig. S5) produces an average model for the study region (Fig. 3d). The resulting model appears quite smooth with a clear Moho at a depth of ~40 km.

In order examine the lateral extent of structures across the study area, the RFs were geographically stacked into common conversion point (CCP) bin (CCP; Dueker and Sheehan, 1997). We use our regional Vs model to migrate the RFs from time to depth by calculating the delay time (Gurrola et al., 1994) of the RF to the stacking bins at each depth increment along its path through the 3D volume of CCP stacking bins. The RFs are then resampled by identifying the signal at the appropriate

arrival time to assign to each sampling depth. All of the RFs that sample each CCP point are then binned and stacked. The bin size can be adjusted to increase or reduce the number of RFs stacked into one bin. Using smaller bins allows for sensitivity to smaller lateral variations, while also limiting the number of traces contributing to each stacking point. The bin size used here was selected such that observed small-scale structural variations could be sufficiently sampled to be able to assess whether they are robust features and required by the data. Only bins sampled by ≥ 10 traces are included in the CCP stacks.

The uncertainties on the velocity model lead to differences of up to 1 s during the time to depth migration (Gurrola et al., 1994). Using these values, and an average crustal shear-wave velocity of 3.5 km/s, causes an uncertainty of ~4 km in our crustal thickness measurements.

3.4. Gravity data

Taking advantage of the strong relationships between rock composition, seismic velocity and rock density (e.g. Ludwig et al., 1970; Christensen and Mooney, 1995; Brocher, 2005), we decided to further validate the seismic wave velocity structure obtained by the joint inversion of RFs and SW dispersion data by inverting gravity data observed at the surface.

In this work, we use a combination of terrestrial gravity measurements, part of the South America Gravity Project database (Pacino, 2007) and satellite observations from the GOCO 05s project (Mayer-
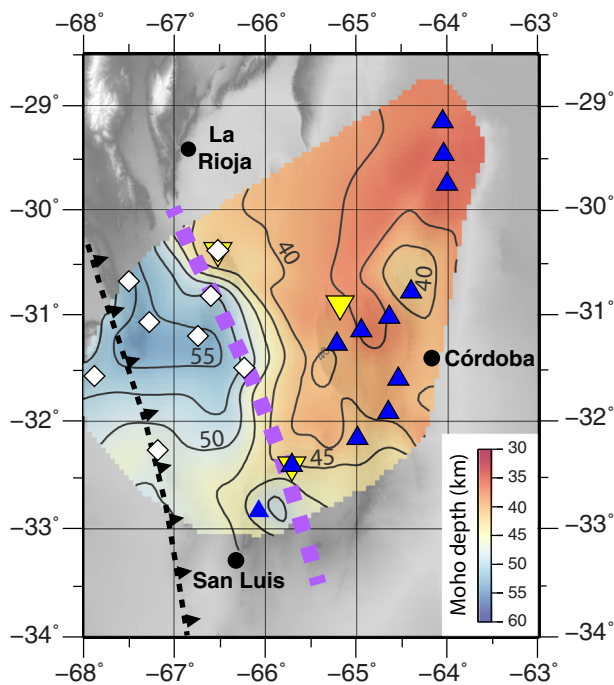
Fig. 5. Map showing the variation of the Moho depth inferred from the CCP stack amplitudes. The black dashed line shows the inferred VFLH fault at the surface as in Ortiz et al. (2015), extending to the southeast. The dashed purple line shows the NW-SE general trend of the Moho step. Note the similar orientation between this Moho step and the VFLH lineament. (For interpretation of the references to color in this figure legend, the reader is referred to the web version of this article.)

Gürr et al., 2015) with nominal grid spacing of 10 km (Alcacer, 2018). We considered 192 gravity measurements that span the study region along two, nearly E-W profiles (Fig. 2b).

The theoretical gravity response is computed using the Somigliana expression with parameters corresponding to the 1980 Reference Geodetic System (GRS1980, Hofmann-Wellenhof and Moritz, 2006). The Bouguer anomaly is then calculated applying free-air correction and taking into account the Earth curvature (LaFehr, 1991). Also, we use the 90 m resolution digital elevation model from the Shuttle Radar Topography Mission (SRTM90 - Farr et al., 2007) to correct the effects of the topography. We use the GM-SYS software (http://geosoft.com/products/gm-sys) to compute the gravity response for two-dimensional bodies following the methodology described in Talwani et al. (1959). The crustal geometry used to compute the complete Bouguer anomaly is derived from the velocity structure obtained by the joint inversion. Density values for each layer are estimated using the Vs from our joint inversion results and density-Vs scaling relations based on the Nafe-Drake empirical relationship (Ludwig et al., 1970) that have been recalibrated by Brocher (2005) to consider different types of crustal lithologies.

4. Results and interpretations

4.1. Crustal discontinuities

The CCP stacks presented here come from two sections from the CCP volume (Figs. 2b & 4). The stacks from both cross-sections possess strong positive arrivals that span across much of the study region. This arrival lies at a depth of 35–40 km depth beneath the Sierras de Córdoba along the eastern portion of the ESP region and at 50–55 km depth at the transition to the WSP region.

Such signal has been observed in previous RF studies beneath the Sierra de Córdoba (Perarnau et al., 2012) and more to the west beneath

the WSP (Calkins et al., 2006; Perarnau et al., 2010; Gans et al., 2011) and confirmed by P- and S-wave travel time inversions (Venerdini et al., 2016). In all cases, it has been interpreted as the Moho signal. Moho depths found in this work are in good agreement with those previous observations. However, our RF images show with more details the westward deepening of the Moho. Although we acknowledge that the seismic raypaths have lower concentration due to sparser station coverage, one striking observation is the significant variation in Moho depth at about 66°W dropping from ~50 km depth in the west to ~40 km depth in the east, a feature particularly well observed in the northern (P1) cross-section (Figs. 2b, 4a & b).

We suggest that this Moho offset correlates with the transition in depth between the Pampia terrane (east) and the Cuyania terrane (west). At the surface, at about 67.5°W, the same transition corresponds to the suture zone that controls the uplift of the Sierra de VFLH, likely bounded by a reverse fault in its western flank (Ramos et al., 2002; Ortiz et al., 2015; Ahumada et al., 2017) (Fig. 2a). The earliest evidence of activity for this structure dates back to the Cambrian when the Cuyania terrane docked to the western margin of Gondwana (Mulcahy et al., 2007; Ramos et al., 2010). This structure later accompanied regional extension during the subsequent breakup of Gondwana (late Triassic to early Cretaceous) (Ramos et al., 2002) and thus would have recently been reactivated in reverse motion during the Andean compression (Neogene) resulting in the uplift of the Sierra de VFLH (Ortiz et al., 2015).

At a regional scale, the surface deformation velocity field from GPS geodesy (Brooks et al., 2003) shows quite constant velocity vectors of similar orientation from the Chilean coast to the Argentine back arc region (at ~68°W or ~400 km east from the trench). Further east, GPS-measured velocities seem to decrease dramatically. The authors have interpreted this important drop in GPS velocity by the presence of a major structure accommodating shortening between two rigid blocks: the Cuyania and Pampia terranes. Other studies showed that the crustal seismicity in the flat slab region is mostly distributed along the sutures that separate the different terranes (Alvarado et al., 2005, 2009; Ammirati et al., 2015, 2016). Low temperature thermochronology, seismicity and neotectonic studies by Ortiz et al. (2015) provide evidence for an active faulting zone to the west of the northern Sierra de VFLH with structures dipping to the east and likely accommodating EW crustal shortening, in good agreement with the aforementioned surface GPS measurements.

For each bin (Fig. 2b), we retrieved the depth corresponding to the RF positive signal associated with the Moho. Depth variations between the obtained values are interpolated by triangulation (Watson, 1982). These CCP stack-derived Moho depths allow to regionally visualize the Moho topography (Fig. 5). Also observed in Fig. 4, the crust is in general thicker to the west with a step at ~66°W. Interestingly, we note a NW-SE trend for this Moho step that seems to align with the proposed suture zone between the Cuyania and Pampia terranes (Figs. 2a & 5). We believe that this structure is responsible for the uplift of the Sierra de VFLH as constrained by Ortiz et al. (2015) and likely accommodates compressive motions between the Pampia and Cuyania terranes all the way down to the Moho as a major, crustal-scale structure (Fig. 4b).

Our CCP stacks (Figs. 4a & b) also display a small Moho offset at ~64.5°W. This vertical shift in the Moho signal, also identified by Perarnau et al. (2012) in the same area could mark the separation at depth between the Pampia terrane (west) from the Rio de La Plata craton (east) since it appears to coincide with a major contact inferred at the surface (Rapela et al., 2011). Care must be taken interpreting this ~5 km Moho offset, because it is close to the depth uncertainty associated with the RF stacks presented here.

Evidence for crustal layering at shallower levels comes in a series of laterally continuous discontinuities at mid-crustal depths, Beneath the WSP we observe 2 mid-crustal discontinuities at ~15 and 35 km (Fig. 4a). These RF arrivals appear at similar depths to structures that has previously been interpreted to be regional décollements (e.g.

Calkins et al., 2006; Perarnau et al., 2010). These mid-crustal structures may be zones of ongoing deformation as they lie near regions of mid-crustal seismicity (Regnier et al., 1994) just as identified further east beneath the Sierra de Córdoba (Richardson et al., 2012). These observations are suggestive of recent, and possibly ongoing, uplift of the Sierra de Pie de Palo (Ramos et al., 2002; Alvarado et al., 2005; Siame et al., 2015).

Further to the east, the crust beneath the Sierra de Córdoba (ESP) is characterized by the presence of two shallower discontinuities in seismic velocities at ~10 and ~25 km depths (Fig. 4b). The 25 km discontinuity is consistent with earthquake locations by Richardson et al. (2012) as they concluded that most of the seismic activity in this sector was horizontally distributed within a region between 15 and 25 km depths. This observation was in good agreement with Perarnau et al.'s (2012) suggestion of basement faulting reaching a décollement level at 20 km depth, approximately. Images in Fig. 4b and d clearly identify this décollement level beneath the ESP. Richardson et al. (2012) also found a cluster of very shallow seismicity (focal depths < 10 km) beneath the Sierras de Córdoba (Fig. 2a) likely associated to the boundary between the Pampia terrane and the Rio de la Plata craton (Fig. 4b). Because the Rio de la Plata craton to the east of Sierras de Córdoba has not been well sampled seismically, the eastward continuation of seismic activity to the east cannot be ruled out.

The presence of a discontinuity in seismic velocities at ~10 km depth (between 65°W and 65.5°W in Fig. 4b) remains unclear. But, because of the irregular form of this discontinuity it could be related to very local heterogeneities such as changes of lithology as further discussed below.

4.2. Vs and composition of crustal rocks

Our joint inversion of RF and SW dispersion data allows constraining absolute S-wave velocities (Figs. 6 & S5). Overall, the velocity structure obtained in this is in good agreement with observations from previous tomographic studies. However, our images present an improved vertical resolution compared to studies that relied on SW and ANT alone (e.g. Porter et al., 2012; Ward et al., 2013), which allow the interpretation of crustal features. Extrapolating our velocity models into 2-D cross-sections, we are able to relate crustal shear wave velocity variations with crustal rock compositions based on a series of geological and geophysical observations performed on typical crustal rocks (Christensen and Mooney, 1995; Christensen, 1996).

Low shear wave velocities are found at very shallow depths in sectors of sedimentary basins with low elevation (between longitudes of 65.5° and 66.5°W in Figs. 6a & b). According to Brocher (2005), such low velocity values are generally associated with the presence of sedimentary rocks. In our case, regions at shallow depths (< 5 km depth) with low velocities (Vs < 3.2 km/s) coincide with areas of Quaternary basins (Lucero-Michaut et al., 1995). Shear wave velocity increases between 5 and ~25 km depths to reach an average value of 3.5–3.6 km/s, which is typically observed in quartz-enriched lithologies such as gneisses, granites and granodiorites (Christensen and Mooney, 1995; Christensen, 1996). This observation agrees with the composition of exposed Cambrian/Ordovician basement rocks forming the ESP (Lucero-Michaut et al., 1995; Martino, 2003) (Fig. 2a) and thus characterizes the Pampia basement. A granitic crust is typically composed of ~60% SiO_2 (Pakiser and Robinson, 1966; Taylor and McLennan, 1981; Christensen and Mooney, 1995). Depending on P-T conditions, quartz begins to behave plastically at depths ranging from 15 to 20 km (Scholz, 1990). The increase in S-wave velocity at 20–25 km depths with values > 3.6 km/s is thus compatible with a brittle-ductile transition at this depth for a crust of a more granitic composition. It also agrees with the bottom of the seismic zone observed by Richardson et al. (2012) and the décollement level at ~25 km inferred by Perarnau et al. (2012).

A closer look at the crustal velocity variations at shallower levels, allows for a localized decrease in Vs to be identified (low velocity zones

– LVZ). This feature is particularly visible beneath stations ESP07, ESP08 and ESP12 near a depth of 10 km. Comparing the Vs model produced here to our CCP RF stacks (Figs. 2b, 4 & 6), we are able to identify that this LVZ lines up with a shallow discontinuity. The geologic settings of these LVZ correspond to the locations of the Pocho Volcanic Field to the north and the El Morro Volcanic Field to the south (Fig. 2b). Volcanism in this region includes normal to high-K basalts and shoshonites (Kay and Gordillo, 1994; Urbina et al., 1997), which have been attributed to the arrival of the shallowly dipping slab. The S-wave velocities characterizing these LVZs (3.1 to 3.3 km/s) agree with velocities found in andesites and trachyandesites (Christensen and Mooney, 1995; Christensen, 1996). The compositions are compatible with the minerals within the basalts observed at the surface (High SiO_2 and K contents). Hence, those localized LVZs at ~10 km depth could correspond to the presence of old magmatic chambers from which those basalts are derived.

For depths > 25 km, on the eastern side of our cross-sections (longitude lower than 65.5°W), S-wave velocities gradually increase up to 4.3 km/s. We interpret the Vs = 4.3 km/s contour line (Fig. 6) as the transition velocity from lower crust to upper mantle although wave velocity variations from ANT (Porter et al., 2012) suggest that the Nazca plate is dehydrating beneath the ESP, which would result in slower Vs than expected for upper mantle velocities. It is worth to note that the 4.3 km/s contour line depth matches quite well the Moho depth extrapolated from the CCP stacks (Fig. 6). Shear wave velocities > 4.3 km/s are interpreted as upper mantle velocities.

To the west of 65.5°W, the lower crust wave velocities between 30 and 40 km depths (Fig. 6), appear to be quite higher (3.7 < Vs < 3.9 km/s) and are generally associated with mafic lithologies such as rocks in the greenschists facies and mafic granulites (Christensen, 1996). Higher velocities (Vs ~ 4.0 km/s) could be explained by the presence of eclogites although, probably in small fractions. This high velocity zone (HVZ) seems to be laterally bounded to the east by the Moho step observed on the CCP stacks images at ~66°W (Fig. 4). Previous studies of crustal wave velocity structure calibrated with petrological observations beneath the Precordillera and the WSP (e.g. Pérez Luján et al., 2015; Ammirati et al., 2015; Ahumada et al., 2017) have shown that the Cuyania basement presents a much more mafic composition with a partially eclogitized lower-crust. The velocity structure observed beneath stations NOQE, ABRA, ESP11 and ESP12 (Figs. 2b, 6c), suggests the underthrusting of the partially eclogitized lower crust of the Cuyania terrane beneath the quartz-rich upper crust along the VFLH structure as inferred from our RF images. Both the abnormally high values of crustal thickness (world average: ~40 km – Christensen and Mooney, 1995) and the strong contrast in wave velocities between upper and lower crust on the western part of the ESP (west of 65.5°W) can be explained by partial eclogitization in the lower crust.

4.3. Crustal densities

In order to further investigate if the crustal geometry and rock composition inferred from our seismic data match gravimetric observations at the surface we built two 2D crustal density models (Fig. 7). The first model (G1), has been realized along the seismic cross section P1. The second density model (G2), runs along latitude 31.5°. We chose to model the crustal density for these two cross sections because they present a general orientation nearly perpendicular to the regional tectonic features (Fig. 2a).

Our models include an average crustal structure and have been modified to take into account lower crustal layering deeper than 30 km to the west of 65°W and the presence of localized high density magmatic rocks at ~10 km depth in the Pampia terrane. The geometry of the key features are based on the seismic images (Fig. 6a) and adjusted to fit the observed Bouguer anomaly. Constraining the geometry of the density model with our seismic observations contributes to increase its robustness, since the gravity data can usually be adjusted by a large
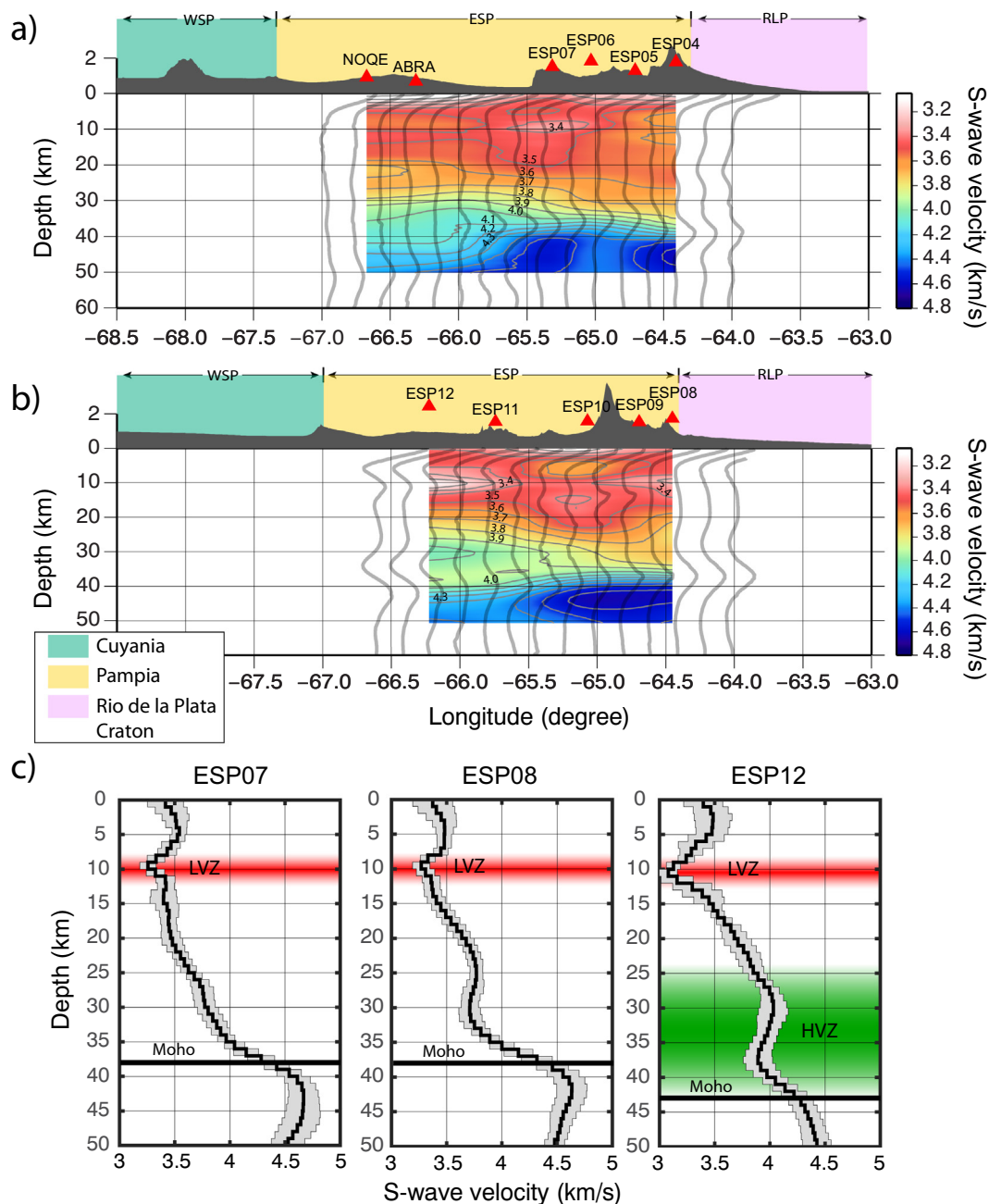
Fig. 6. a) and b) Joint inversion results for cross-sections P1 and P2, respectively (see Fig. 2b for location). Low velocities appear in red colors, high velocities appear in green/blue colors. Contour spacing is 0.1 km/s (see main text for details of the joint inversion process). CCP stacked RFs are superimposed over S-wave velocities as grey lines. c) One-dimension velocity model for stations ESP07, ESP08 and ESP12 (see Fig. 2b for location). Note S-wave velocity decreases around 10 km depth. Also note the relatively high lower crust S-wave velocity for station ESP12 between 25 and 40 km depths. (For interpretation of the references to color in this figure legend, the reader is referred to the web version of this article.)

amount of different models. Each layer is set to be homogenous with densities of 2700 kg/m³ for the upper crust, 2830 kg/m³ for the middle crust, and 3050 kg/m³ for the lower crustal layer. These values were determined using the Vs from our absolute velocity cross-sections (Fig. 6) and density-Vs scaling relations based on the Nafe-Drake empirical relationship (Ludwig et al., 1970; Brocher, 2005). Sedimentary basins were also taken into account to further reduce the misfit between modeled and observed gravity data. The residuals between observed and modeled gravity in the final models is 2.5 mGal.

Depocenters located east of the Sierra de Córdoba and between the Sierra de VFLH and Sierra de Chepes (Figs. 2a & 7), have been modeled as shallow (< 3 km depth) bodies with a density of 2320 kg/m³, a value

characteristic of sedimentary fills (Mescua et al., 2016). The magmatic bodies have a density of 2920 kg/m³ which corresponds to the density observed for trachyandesites and trackybasalts found in the Sierras Pampeanas (Krapovickas and Tauber, 2016).

In our models, the Moho depth generally decreases from west to east, with values ranging from ~50 km for the western part of the Pampia terrane to ~33 km for the Rio de la Plata craton. We can observe that the Moho depth in the density models (Fig. 7) matches quite well the CCP-derived Moho depth variations (Fig. 5). An interesting observation is that we had to include a small crustal root beneath the Sierras de Córdoba (particularly well visible in G2) in order to locally fit the gravimetric anomaly observed in the Sierras de Córdoba. This
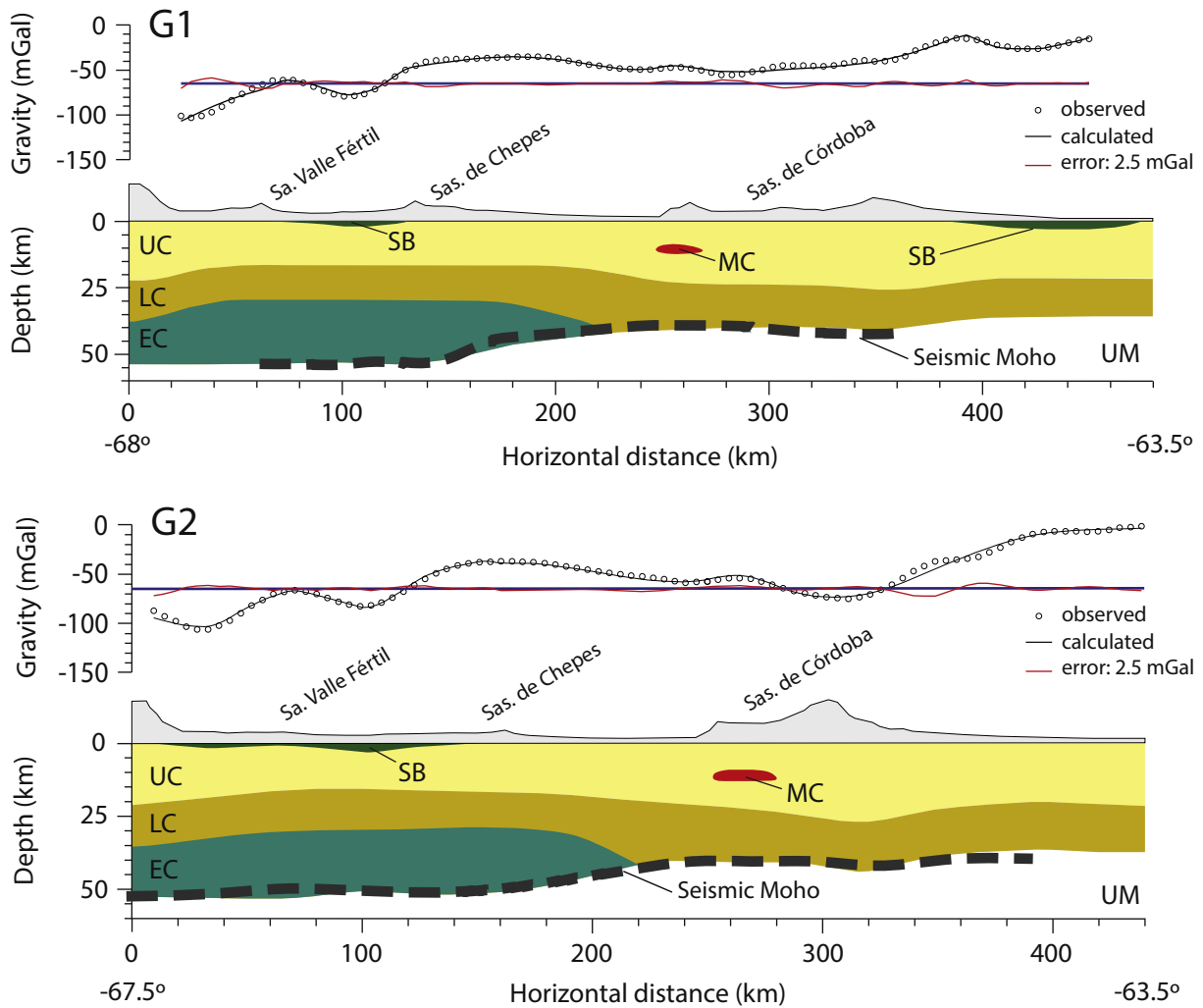
Fig. 7. Gravity and density cross-sections (see Fig. 2b for location). The forward models fits the gravity data observed at the surface. The blue line represents the perfect fit between observed and modeled gravity. The crustal thickness and overall geometry have been constrained from our seismic results (Figs. 4 & 6). UC: upper crust; LC: lower crust; EC: partially eclogitized crust; UM: upper mantle; MC: magma chamber; SB: sedimentary basin. The corresponding densities have been chosen considering the Vs obtained from our joint RF-SW inversion and Vs-density scaling (Ludwig et al., 1970). For comparison, the dashed dark grey lines show the Moho depth along the corresponding cross-section, inferred from CCP stacked RFs (Fig. 5). (For interpretation of the references to color in this figure legend, the reader is referred to the web version of this article.)
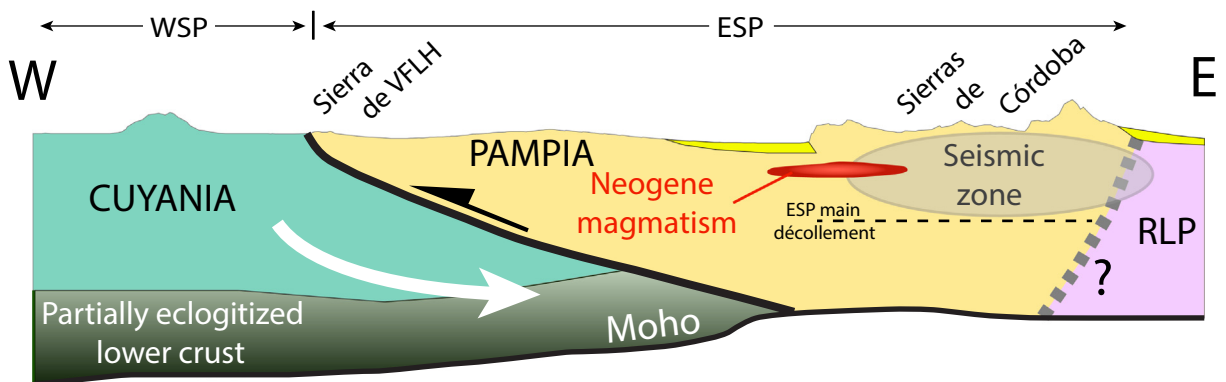

Fig. 8. Schematic E-W profile across our study area. We suggest an east dipping structure that accommodates crustal shortening between Pampia and Cuyania terranes. Due to differences in rock composition and density we infer that the Cuyania terrane is underthrusting the Pampia terrane in its western sector. We also suggest the presence of a small Moho depth variation beneath the Sierras de Córdoba (easternmost part of the ESP) possibly related to the transition between the Pampia terrane and the Rio de la Plata craton (RLP). Our results provide evidence for the presence of magma chambers at about 10 km depth likely related to Neogene magmatism in the ESP (e.g. Kay and Gordillo, 1994; Urbina et al., 1997).

observation coincides with the Moho perturbation observed in the CCP stacks for this area (Figs. 4a & b) as identified by Richardson et al. (2012) and Perarnau et al. (2012). The gravity model presented here strengthens the hypothesis of a change in Moho depth, at the transition between the Pampia terrane (west) and the Rio de la Plata craton (east) (Fig. 8). Additional constraints of the crustal structure of the Rio de la Plata craton would allow for this hypothesis to be further tested.

5. Conclusions

Jointly inverting RF and surface wave observations, we produced a detailed model of the crust of the WSP to the ESP (Fig. 8). Combining this model with additional constraints from gravity and petrologic modeling has helped to improve our understanding of structures within the region and the processes that contributed to its formation. Our results show changes in Moho depths with a NW-SE regional trend that divides the study area with a deeper Moho (> 45–50 km depth) in the west in comparison with a shallower Moho (35–40 km depth) in the eastern region. This trend shows a good correlation with the Cuyania-Pampia suture zone in the western Sierras Pampeanas. Our observations suggest that this structure extend at depth and delimitates the Cuyania-Pampia transition down to 35–45 km depths, beneath the eastern Sierras Pampeanas. Shear wave velocities (< 3.6 km/s) found in this work are compatible with quartz-enriched lithology characterizing the Pampia terrane whereas the western basement presents high lower-crust wave velocities (> 3.8 km/s) suggesting the presence of mafic-ultramafic material, characteristic of the Cuyania terrane. A crustal density model derived from the wave velocity structure allowed us to explain the observed gravity anomalies. Our model provides evidence for the underthrusting of the partially eclogitized Cuyania lower crust beneath the Pampia terrane. We believe that the Sierra de Valle Fértil-La Huerta structure is accommodating west to east underthrusting of the Cuyania terrane beneath the Pampia terrane. Interestingly, we are able to observe very localized crustal low-velocity zones beneath the El Pocho and El Morro volcanic fields (Sierras de Córdoba and Sierra de San Luis, respectively), at ~10 km depth. The low wave velocities estimated for those areas may be related to the presence of old magma chambers in good agreement with the composition of the volcanic rocks exposed at the surface. Our results are summarized in Fig. 8.

Acknowledgments

Appendix A. Supplementary data

Supplementary data to this article can be found online at https://doi.org/10.1016/j.tecto.2018.05.015.

References

Ahumada, M.F., Castro de Machuca, B., Alvarado, P., Ammirati, J.B., López, M.G., 2017. Modelo petrofísico del borde oriental de las sierras de Valle Fértil-La Huerta, Argentina a partir de datos sísmicos y petrológicos. Rev. Mex. Cienc. Geol. 34 (1), 1–11. http://satori.geociencias.unam.mx/34-1/(01)Ahumada.pdf.

Alcacer, J.M., 2018. Modelos globales de gravedad, su uso en estudios tectónicos. Universidad Nacional de San Juan, San Juan, Argentina (dissertation (PhD)).

Alvarado, P., Beck, S., Zandt, G., Araujo, M., Triep, E., 2005. Crustal deformation in the south-central Andes backarc terranes as viewed from regional broad-band seismic waveform modeling. Geophys. J. Int. 163 (2), 580–598. http://dx.doi.org/10.1111/j.1365-246X.2005.02759.x.

Alvarado, P., Beck, S., Zandt, G., 2007. Crustal structure of the south-central Andes Cordillera and backarc region from regional waveform modelling. Geophys. J. Int. 170, 858–875.

Alvarado, P., Pardo, M., Gilbert, H., Miranda, S., Anderson, M., Saez, M., Beck, S., 2009. Flat-slab subduction and crustal models for the seismically active Sierras Pampeanas region of Argentina. In: Kay, S., Ramos, V., Dickinson, W. (Eds.), MWR204: Backbone of the Americas: Shallow Subduction, Plateau Uplift, and Ridge and Terrane Collision, pp. 261–278. http://dx.doi.org/10.1130/2009.1204(12).

Ammirati, J.-B., Alvarado, P., Perarnau, M., Saez, M., Monsalvo, G., 2013. Crustal structure of the Central Precordillera of San Juan, Argentina (31°S) using teleseismic receiver functions. J. S. Am. Earth Sci. 46, 100–109. http://dx.doi.org/10.1016/j.jsames.2013.05.007.

Ammirati, J.-B., Alvarado, P., Beck, S., 2015. A lithospheric velocity model for the flat slab region of Argentina from joint inversion of Rayleigh wave phase velocity dispersion and teleseismic receiver functions. Geophys. J. Int. 202, 224–241. http://dx.doi.org/10.1093/gji/ggv140.

Ammirati, J.-B., Pérez Luján, S., Alvarado, P., Beck, S., Rocher, S., Zandt, G., 2016. High-resolution images above the Pampean flat slab of Argentina (31–32°S) from local receiver functions: implications on regional tectonics. Earth Planet. Sci. Lett. 450, 29–39. http://dx.doi.org/10.1016/j.epsl.2016.06.018.

Ammon, C.J., Randall, G.E., Zandt, G., 1990. On the nonuniqueness of receiver function inversions. J. Geophys. Res. 95, 15303–15318.

Anderson, M., Alvarado, P., Zandt, G., Beck, S., 2007. Geometry and brittle deformation of the subducting Nazca plate, central Chile and Argentina. Geophys. J. Int. 171, 419–434.

Barazangi, M., Isacks, B.L., 1976. Spatial distribution of earthquakes and subduction of the Nazca plate beneath South America. Geology 4, 686–692.

Booker, J., Favetto, A., Pomposiello, C., 2004. Low electrical resistivity associated with plunging of the Nazca flat slab beneath Argentina. Nature 429, 399–403.

Brocher, T.M., 2005. Empirical relations between elastic wavespeeds and density in the Earth's crust. Bull. Seismol. Soc. Am. 95, 2081–2092. http://dx.doi.org/10.1785/0120050077.

Brooks, B., Bevis, M., Smalley, R., Kendrick, E., Manceda, R., Lauría, E., Maturana, R., Araujo, M., 2003. Crustal motion in the Southern Andes (26°–36°S): do the Andes behave like a microplate? Geochem. Geophys. Geosyst. 4, 1–14.

Cahill, T., Isacks, B.L., 1992. Seismicity and shape of the subducted Nazca plate. J. Geophys. Res. 97 (B12), 17503–17529.

Calkins, J., Zandt, G., Gilbert, H., Beck, S., 2006. Crustal images from San Juan, Argentina, obtained using high frequency local event receiver functions. Geophys. Res. Lett. 33, 1–4. http://dx.doi.org/10.1029/2005GL025516.

Christensen, N.I., 1996. Poisson's ratio and crustal seismology. J. Geophys. Res. 101, 3139–3156. http://dx.doi.org/10.1029/95JB03446.

Christensen, N.I., Mooney, W.D., 1995. Seismic velocity structure and composition of the continental crust: a global view. J. Geophys. Res. 100, 9761–9788. http://dx.doi.org/10.1029/95JB00259.

DeMets, C., Gordon, R.G., Argus, D.F., 2010. Geologically current plate motions. Geophys. J. Int. 181, 1–80.

Dueker, K.G., Sheehan, A.F., 1997. Mantle discontinuity structure from midpoint stacks of converted P to S waves across the Yellowstone hotspot track. J. Geophys. Res. 102, 8313–8327. http://dx.doi.org/10.1029/96JB03857.

Eagar, K.C., Fouch, M.J., 2012. FuncLab: a MATLAB interactive toolbox for handling receiver function datasets. Seismol. Res. Lett. 83 (3), 596–603. http://dx.doi.org/10.1785/gssrl.83.3.596.

Farr, T.G., Rosen, P.A., Caro, E., Crippen, R., Duren, S., Hensley, S., Kobrick, M., Paller, M., Rodriguez, E., Roth, L., Seal, D., Shaffer, S., Shimada, J., Umland, M., Werner, M., Oskin, M., Burbank, D., Alsdorf, D., 2007. The shuttle radar topography mission. Rev. Geophys. 45, 1–33.

Gans, C.R., Beck, S.L., Zandt, G., Gilbert, H., Alvarado, P., Anderson, M., Linkimer, L., 2011. Continental and oceanic crustal structure of the Pampean flat slab region, western Argentina, using receiver function analysis: new high-resolution results. Geophys. J. Int. 186, 45–58. http://dx.doi.org/10.1111/j.1365-246X.2011.05023.x.

Gilbert, H., Beck, S., Zandt, G., 2006. Lithospheric and upper mantle structure of central Chile and Argentina. Geophys. J. Int. 165, 383–398. http://dx.doi.org/10.1111/j.1365-246X.2006.02867.x.

Gordillo, C.E., Linares, A., 1981. Geocronología y petrografía de las vulcanitas terciarias del Departamento de Pocho. Provincia de Córdoba. Rev. Asoc. Geol. Argent. 36, 380–388.

Gurrola, H., Minster, J.B., Owens, T., 1994. The use of velocity spectrum for stacking receiver functions and imaging upper mantle discontinuities. Geophys. J. Int. 117, 427–440. http://dx.doi.org/10.1111/j.1365-246X.1994.tb03942.x.

Herrmann, R.B., 1973. Some aspects of band-pass filtering of surfacewaves. Bull. Seismol. Soc. Am. 63, 703–711.

Herrmann, R.B., Ammon, C.J., 2002. Computer programs in seismology 3.30: surface

waves, receiver functions and crustal structure. Available at: www.eas.slu.edu/People/RBHerrmann/CPS330.html.

Hofmann-Wellenhof, B., Moritz, H., 2006. Physical Geodesy. Springer-Verlag New York, LLC (403 pp.).

INPRES, 2018. Intituto Nacional de Prevención Sísmica. Terremotos históricos ocurridos en la República Argentina. Available at: http://contenidos.inpres.gov.ar/sismologia/historicos.

Julià, J., Ammon, C.J., Herrmann, R.B., Correig, A.M., 2000. Joint inversion of receiver function and surface wave dispersion observations. Geophys. J. Int. 143, 99–112.

Julià, J., Assumpção, M., Rocha, M.P., 2008. Deep crustal structure of the Paraná Basin from receiver functions and Rayleigh-wave dispersion: evidence for a fragmented cratonic root. J. Geophys. Res. 113, B08318. http://dx.doi.org/10.1029/2007JB005374.

Kay, S., Abbruzzi, J., 1996. Magmatic evidence for Neogene lithospheric evolution of the Central Andean flat-slab between 30 and 32°S. Tectonophysics 259, 15–28. http://dx.doi.org/10.1016/0040-1951(96)00032-7.

Kay, S., Gordillo, C.E., 1994. Pocho volcanic rocks and the melting of depleted continental lithosphere above a shallowly dipping subduction zone in the central Andes. Contrib. Mineral. Petrol. 117 (1), 25–44.

Kennett, B.L.N., Engdahl, E.R., Buland, R., 1995. Constraints on seismic velocities in the Earth from traveltimes. Geophys. J. Int. 122, 108–124.

Krapovickas, J.M., Tauber, A.A., 2016. Estratigrafía de las áreas cumbrales de las Sierras Pampeanas de Córdoba: geocronología, modelo regional, paleoambiente y paleoclima en una región poco conocida de Argentina. Rev. Mex. Cienc. Geol. 33 (1), 105–121.

LaFehr, T.R., 1991. An exact solution for the gravity curvature (Bullard B) correction. Geophysics 56 (8), 1179–1184.

Langston, C.A., 1979. Structure under Mount Rainier, Washington, inferred from teleseismic body waves. J. Geophys. Res. 84, 4749–4762.

Ligorría, J., Ammon, C.J., 1999. Iterative deconvolution and receiver function estimation. Bull. Seismol. Soc. Am. 89, 1395–1400.

Lucero-Michaut, N.H., Gamkosian, A., Jarsun, B., Zamora, Y.E., Sigismondi, M., Caminos, R., Miro, R., 1995. Mapa Geológico de la Province de Córdoba, República Argentina, 1:500,000. Ministerio de Economía y Obras y Servicios Públicos. SEGEMAR, Buenos Aires.

Ludwig, W.J., Nafe, J.E., Drake, C.L., 1970. In: Maxwell, A.E. (Ed.), Seismic Refraction, in the Sea. vol. 4. Wiley-Interscience, New York, pp. 53–84.

Marot, M., Monfret, T., Pardo, M., Ranalli, G., Nolet, G., 2013. A double seismic zone in the subducting Juan Fernández Ridge of the Nazca Plate (32°S), central Chile. J. Geophys. Res. 118 (7), 3462–3475. http://dx.doi.org/10.1002/jgrb.50240.

Martino, R.D., 2003. Las fajas de deformación dúctil de las Sierras Pampeanas de Córdoba: Una reseña general. Rev. Asoc. Geol. Argent. 58 (4), 549–571.

Martino, R.D., Guereschi, A.D., Montero, A.C., 2016. Reactivation, inversion and basement faulting and thrusting in the Sierras Pampeanas de Córdoba (Argentina) during Andean flat-slab deformation. Geol. Mag. 153 (5/6), 962–991. http://dx.doi.org/10.1017/S0016756816000339.

Mayer-Gürr, T., Kvas, A., Klinger, B., Rieser, D., Zehentner, N., Pail, R., Gruber, T., Fecher, T., Rexer, M., Schuh, W.-D., Kusche, J., Martin, B.J., Loth, I., Müller, S., Eicker, A., Schall, J., Baur, O., Höck, E., Krauss, S., Maier, A., 2015. The new combined satellite only model GOCO05s. In: EGU General Assembly, Vienna, Austria, http://dx.doi.org/10.13140/RG.2.1.4688.6807.

McGlashan, N., Brown, L., Kay, S., 2008. Crustal thickness in the central Andes from teleseismically recorded phase precursors. Geophys. J. Int. 175, 1013–1022.

McMechan, G.A., Yeldin, J., 1981. Analysis of dispersive waves by wave field transformation. Geophysics 46, 869–874.

Mescua, J.F., Giambiagi, L., Barrionuevo, M., Tassara, A., Mardonez, D., Mazzitelli, M., Lossada, A., 2016. Basement composition and basin geometry controls on upper-crustal deformation in the Southern Central Andes (30–36° S). Geol. Mag. 153, 945–961.

Miranda, S., Introcaso, A., 1999. Cartas Gravimétricas de la Provincia de Córdoba. Interpretación de la estructura profunda de la Sierra de Córdoba. In: Temas de Geociencia, vol. 1. UNR Editora, Rosario, República Argentina, pp. 45.

Mulcahy, S.R., Roeske, S.M., McClelland, W.C., Nomade, S., Renne, P.R., 2007. Cambrian initiation of the Las Pirquitas thrust of the western Sierras Pampeanas, Argentina: implications for the tectonic evolution of the proto-Andean margin of South America. Geology 35 (5), 443–446. http://dx.doi.org/10.1130/G23436A.1.

Mulcahy, P., Chen, C., Kay, S.M., Brown, L.D., Isacks, B.L., Sandvol, E., Heit, B., Yuan, X., Coira, B.L., 2014. Central Andean mantle and crustal seismicity beneath the Southern Puna plateau and the northern margin of the Chilean–Pampean flat slab. Tectonics 33 (8), 1636–1658. http://dx.doi.org/10.1002/2013TC003393.

Ortiz, G., Alvarado, P., Fosdick, J., Perucca, L., Saez, M., Venerdini, A., 2015. Active deformation in the northern sierra de Valle Fértil, Sierras Pampeanas, Argentina. J. S. Am. Earth Sci. 64 (Part 2), 339–350. http://dx.doi.org/10.1016/j.jsames.2015.08.015.

Otamendi, J.E., Vujovich, G.I., de la Rosa, J.D., Tibaldi, A.M., Castro, A., Martino, R.D., Pinotti, L.P., 2009. Geology and petrology of a deep crustal zone from the Famatinian paleo-arc, Sierras de Valle Fértil and La Huerta, San Juan, Argentina. J. S. Am. Earth Sci. 27 (4), 258–279. http://dx.doi.org/10.1016/j.jsames.2008.11.007.

Pacino, M.C., 2007. Absolute gravity measurements and gravity networks in South America. Nordic J. Surv. Real Estate Res. 4 (2), 59–69.

Pakiser, L.C., Robinson, R., 1966. Composition and evolution of the continental crust as suggested by seismic observations. Tectonophysics 59, 547–557.

Perarnau, M., Alvarado, P., Saez, M., 2010. Estimación de la estructura cortical de velocidades sísmicas en el suroeste de la Sierra de Pie de Palo, Provincia de San Juan. Rev. Asoc. Geol. Argent. 64, 473–480.

Perarnau, M., Gilbert, H., Alvarado, P., Martino, R., Anderson, M., 2012. Crustal structure of the Eastern Sierras Pampeanas of Argentina using high frequency local receiver functions. Tectonophysics 580, 208–217. http://dx.doi.org/10.1016/j.tecto.2012.09.021.

Pérez Luján, S.B., Ammirati, J.-B., Alvarado, P., Vujovich, G.I., 2015. Constraining a mafic thick crust model in the Andean Precordillera of the Pampean flat slab subduction region. J. S. Am. Earth Sci. 64, 325–338. http://dx.doi.org/10.1016/j.jsames.2015.09.005.

Porter, R., Gilbert, H., Zandt, G., Beck, S., Warren, L., Calkins, J., Alvarado, P., Anderson, M., 2012. Shear wave velocities in the Pampean flat-slab region from Rayleigh wave tomography: implications for slab and upper mantle dehydration. J. Geophys. Res. 117. http://dx.doi.org/10.1029/2012JB009350.

Ramos, V.A., 1988. The tectonics of the Central Andes: 30° to 33°S latitude. In: Clark, S.P., Clark Burchfiel, J.B., Suppe, J. (Eds.), Processes in Continental Lithospheric Deformation. Geological Society of America, pp. 31–54.

Ramos, V.A., Cristallini, E.O., Pérez, D.J., 2002. The Pampean flat-slab of the central Andes. J. S. Am. Earth Sci. 15, 59–78.

Ramos, V.A., Vujovich, G., Martino, R., Otamendi, J., 2010. Pampia: a large cratonic block missing in the Rodinia supercontinent. J. Geodyn. 50, 243–255. http://dx.doi.org/10.1016/j.jog.2010.01.019.

Rapela, C.W., Fanning, C.M., Casquet, C., Pankhurst, R.J., Spalletti, L., Poiré, D., Baldo, E.G., 2011. The Rio de la Plata craton and the adjoining Pan-African/brasiliano terranes: their origins and incorporation into south-west Gondwana. Gondwana Res. 20 (4), 673–690. http://dx.doi.org/10.1016/j.gr.2011.05.001.

Regnier, M., Chatelain, J.L., Smalley, R., Ming Chiu, J., Isacks, B.L., Puebla, N., 1992. Seismotectonics of the Sierra de Pie de Palo, a basement block uplift in the Andean foreland, Argentina. Bull. Seismol. Soc. Am. 82, 2549–2571.

Regnier, M., Chiu, J.-M., Smalley, R., Isacks, B.L., Araujo, M., 1994. Crustal thickness variation in the Andean foreland, Argentina, from converted waves. Bull. Seismol. Soc. Am. 84 (4), 1097–1111.

Richardson, T.J., Gilbert, H.J., Anderson, M.L., Ridgway, K.D., 2012. Seismicity within the actively deforming Eastern Sierras Pampeanas, Argentina. Geophys. J. Int. 188, 408–420.

Richardson, T., Ridgway, K.D., Gilbert, H., Martino, R., Enkelmann, E., Anderson, M., Alvarado, P., 2013. Neogene and Quaternary tectonics of the Eastern Sierras Pampeanas, Argentina: active intraplate deformation inboard of flat-slab subduction. Tectonics 32, 1–17. http://dx.doi.org/10.1002/tect.20054.

Scholz, C.H., 1990. The Mechanics of Earthquakes and Faulting. Cambridge University Press, Cambridge (504 pp.).

Siame, L.L., Sérbier, M., Bellier, O., Bourlès, D., Costa, C., Ahumada, E.A., Gardini, C.E., Cisneros, H., 2015. Active basement uplift of Sierra de Pie de Palo (Northwestern Argentina): rates and inception from 10Be cosmogenic nuclide concentrations. Tectonics 34, 1129–1153. http://dx.doi.org/10.1002/2014TC003771.

Siegesmund, S., Steenken, A., Martino, R., Wemmer, K., López de Luchi, M., 2010. Time constraints on the tectonic evolution of the Eastern Sierras Pampeanas (Central Argentina). Int. J. Earth Sci. (Geologische Rundschau) 99, 1199–1226.

Snyder, D.B., Ramos, V.A., Allmendinger, R.W., 1990. Thick-skinned deformation observed on deep seismic reflection profiles in Western Argentina. Tectonics 9 (4), 773–788.

Stauder, W., 1973. Mechanism and spatial distribution of Chilean earthquakes with relation to subduction of the oceanic plate. J. Geophys. Res. 78, 5033–5061. http://dx.doi.org/10.1029/JB078i023p05033.

Talwani, M., Worzel, J.L., Landisman, M., 1959. Rapid gravity computation for two-dimensional bodies with application to the Mendocino submarine fracture zone. J. Geophys. Res. 64 (1), 49–59.

Taylor, S.R., McLennan, S.M., 1981. The composition and evolution of the continental crust; rare earth element evidence from sedimentary rocks. Philos. Trans. R. Soc. Lond. A 301, 381–399.

Urbina, N., Sruoga, P., Malvicini, L., 1997. Late Tertiary gold-bearing volcanic belt in the Sierras Pampeanas of San Luis, Argentina. Int. Geol. Rev. 39, 287–306.

Venerdini, A., Sánchez, G., Alvarado, P., Bilbao, I., Ammirati, J.-B., 2016. Nuevas determinaciones de velocidades de ondas P y ondas S para la corteza sísmica del terreno Cuyania en el retroarco andino. Rev. Mex. Cienc. Geol. 33 (1), 59–71.

Wagner, L.S., Beck, S., Zandt, G., 2005. Upper mantle structure in the south central Chilean subduction zone (30° to 36°S). J. Geophys. Res. 110. http://dx.doi.org/10.1029/2004JB003238.

Ward, K.M., Porter, R.C., Zandt, G., Beck, S.L., Wagner, L.S., Minaya, E., Tavera, H., 2013. Ambient noise tomography across the Central Andes. Geophys. J. Int. 194, 1559–1573. http://dx.doi.org/10.1093/gji/ggt166.

Watson, D.F., 1982. Acord: automatic contouring of raw data. Comput. Geosci. 8, 97–101.

Yáñez, G., Cembrano, J., Pardo, M., Ranero, C., Selles, D., 2002. The Challenger-Juan Fernández – Maipo major tectonic transition of the Nazca–Andean subduction system at 33–34°S: geodynamic evidence and implications. J. S. Am. Earth Sci. 15, 23–38.